Supporting Information

Tunable Pseudocapacitance in 3D $TiO_{2-\delta}$ Nanomembranes Enabling Superior Lithium Storage Performance

Shaozhuan Huang,[,†] Lin Zhang,[*,†] Xueyi Lu,[†] Lifeng Liu,[‡] Lixiang Liu,[†] Xiaolei Sun,[†] Yin Yin,[†] Steffen Oswald,[∥] Zhaoyong Zou,[#] Fei Ding[†] and Oliver G. Schmidt[†,§]*

[†]Institute for Integrative Nanosciences and [∥]Institute for Complex Materials, IFW Dresden, Helmholtzstraße 20, Dresden 01069, Germany

[‡]International Iberian Nanotechnology Laboratory (INL), Av. Mestre Jose Veiga, 4715-330, Braga, Portugal

[#]Department of Biomaterials, Max Planck Institute of Colloids and Interfaces, Potsdam 14424, Germany

[§]Material Systems for Nanoelectronics, Technische Universität Chemnitz, Chemnitz, Germany

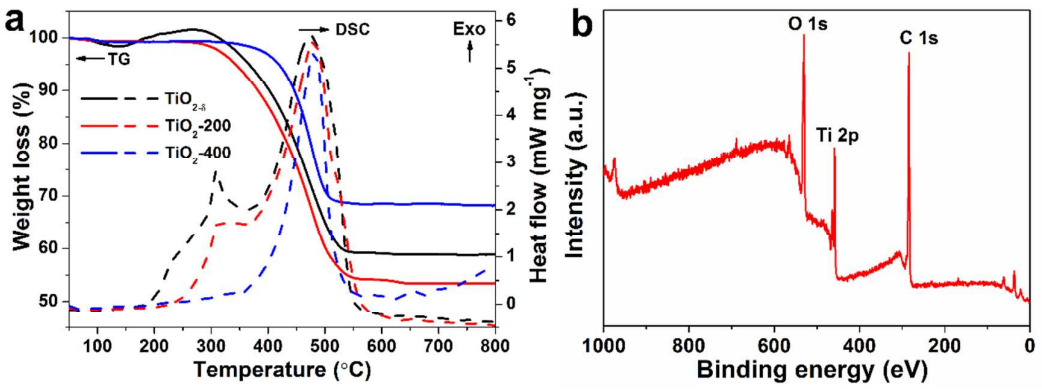

Figure S1. (a) TG/DSC analysis of the $TiO_{2-\delta}$, TiO_2-200 and TiO_2-400, (b) Survey scan of XPS of $TiO_{2-\delta}$.

The $TiO_{2-\delta}$ sample used for TG/DSC test contains some content of photoresist and the TG/DSC was carried out under O_2 atmosphere at a temperature ramping rate of 5 °C min^{-1}. The XPS spectrum demonstrates the existence of large amount of photoresist in the $TiO_{2-\delta}$ sample (Figure S1b). As for the $TiO_{2-\delta}$, the first small weight loss from 80 to 140 °C may be originated from the desorption of physically absorbed water. Then a gently weight gain (3.2%) can be observed from 150 to 290 °C accompanying with a weak and broad exothermic peak around 240 °C, corresponding to the oxidation of the $TiO_{2-\delta}$ with oxygen deficiency. Another sharp exothermic peak around 306 °C with no weight loss corresponds to the phase transition from amorphous to the tetragonal anatase structure.[1] Subsequently, a big weight loss (42.897%) can be observed from 300 to 550 °C, corresponding to the thermal decomposition of photoresist. If we exclude the mass of photoresist, the minimum amount of oxygen deficiencies in $TiO_{2-\delta}$ is calculated to be 5.31%. As for TiO_2-200, which is obtained by annealing the $TiO_{2-\delta}$ at 200 °C for 6 h, the TG plot does not show weight gain from 150 to 300 °C, indicating that nearly no Ti^{3+} and oxygen deficiency exist in this sample, consistent with the XPS result in Figure 2c. Also, the weak exothermic peak around 306 °C corresponds to the phase transition from amorphous to the tetragonal anatase structure, and the weight loss from 300 to 550 °C corresponds to the thermal decomposition of photoresist. Because the photoresist starts to decompose from 300 °C, it is fully preserved in the TiO_2-200 sample. Therefore, from the TG plots of $TiO_{2-\delta}$ and TiO_2-200, the amount of oxygen deficiencies in $TiO_{2-\delta}$ can be estimated to be 7.66%. So the oxygen deficiency of the $TiO_{2-\delta}$ should be 5.31%-7.66%. As for TiO_2-400 (anatase phase), no phase transition at 306 °C is observed, but the weight loss from 400 to 550 °C is visible, corresponding to the thermal decomposition of residual photoresist.

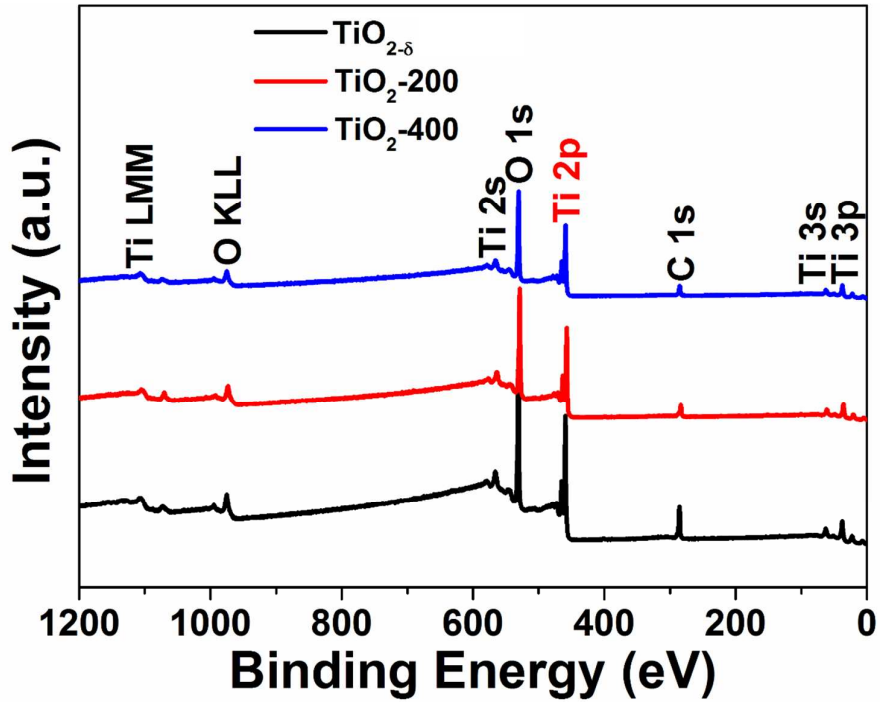

Figure S2. Survey scan of XPS of $TiO_{2-\delta}$, TiO_2-200 and TiO_2-400.

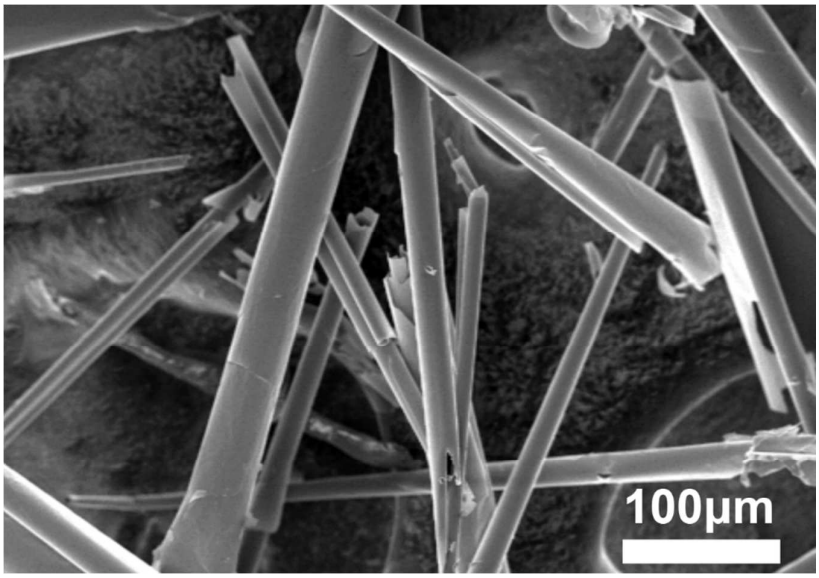

Figure S3. Low magnification SEM image of $TiO_{2-\delta}$.

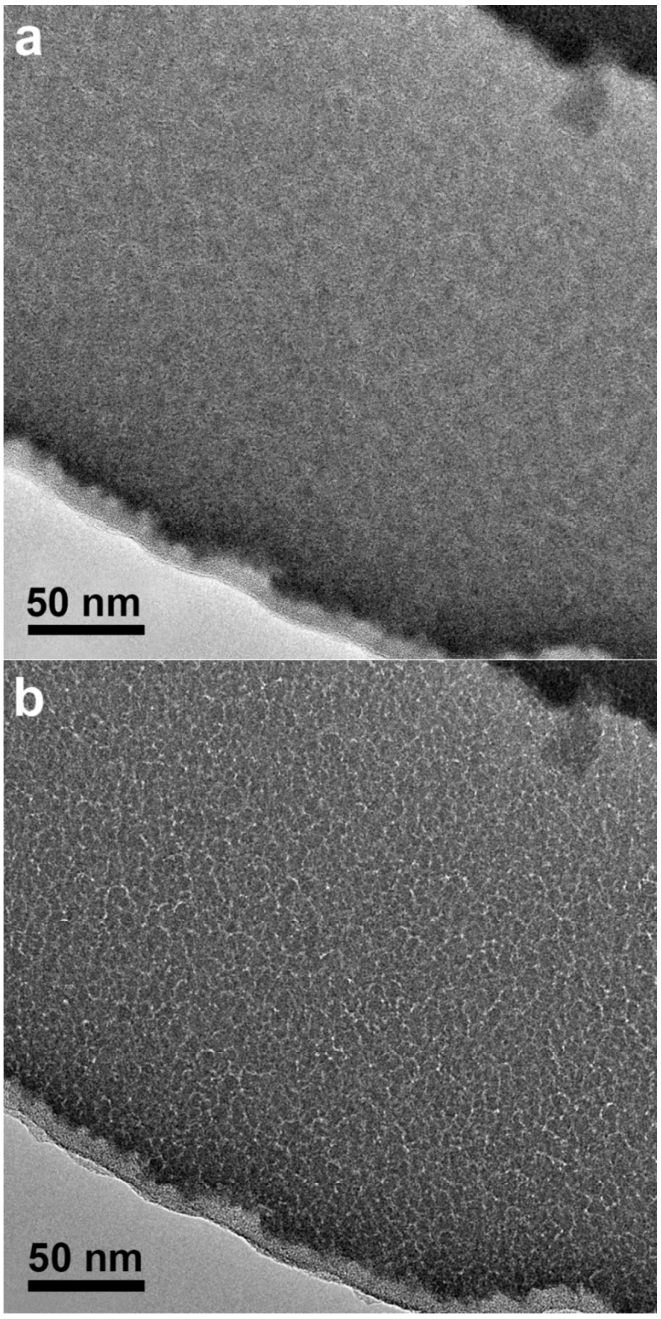

Figure S4. TEM images of the $TiO_{2-\delta}$: (a) focused image, (b) over-focused image.

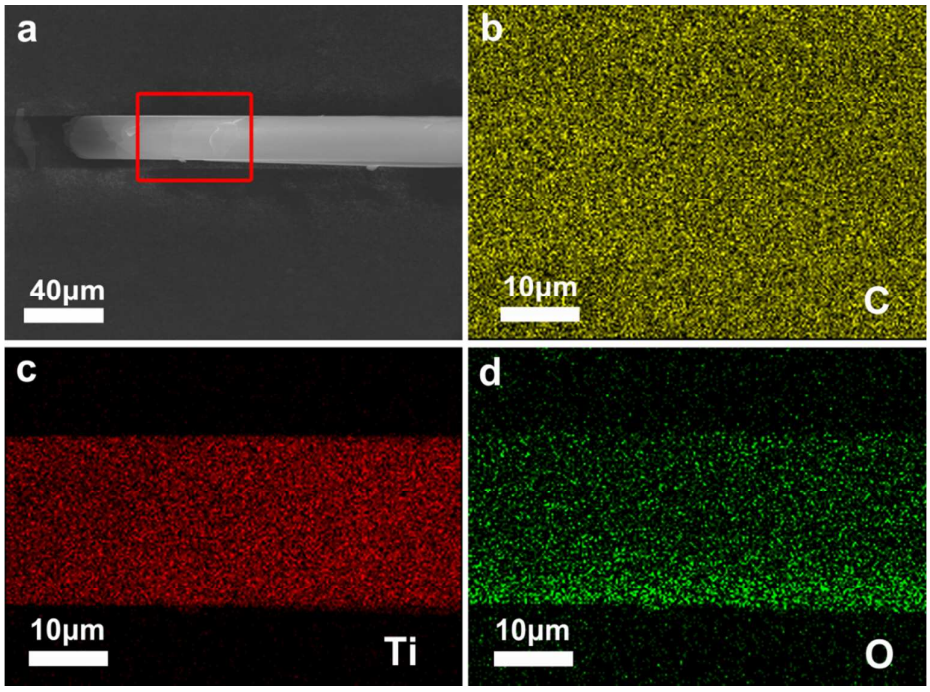

Figure S5. SEM elemental mapping images: (a) SEM image, (b) C, (c) Ti, (d) O. The carbon signals are from the conducting resin substrate.

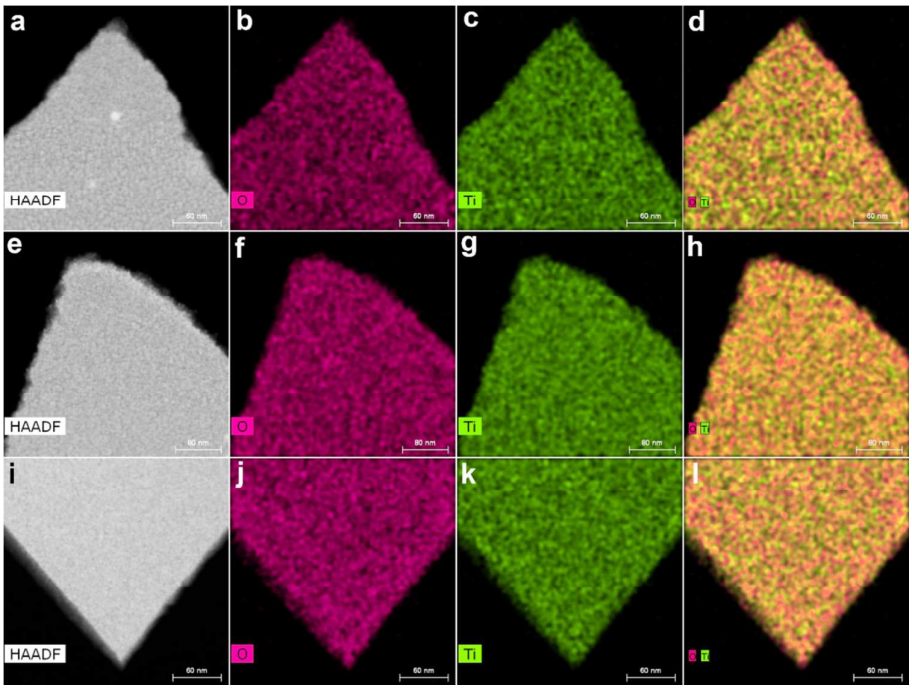

Figure S6. STEM-EDS elemental mapping images: $TiO_{2-\delta}$ (a-d), TiO_2-200 (e-h) and TiO_2-400 (i-l).

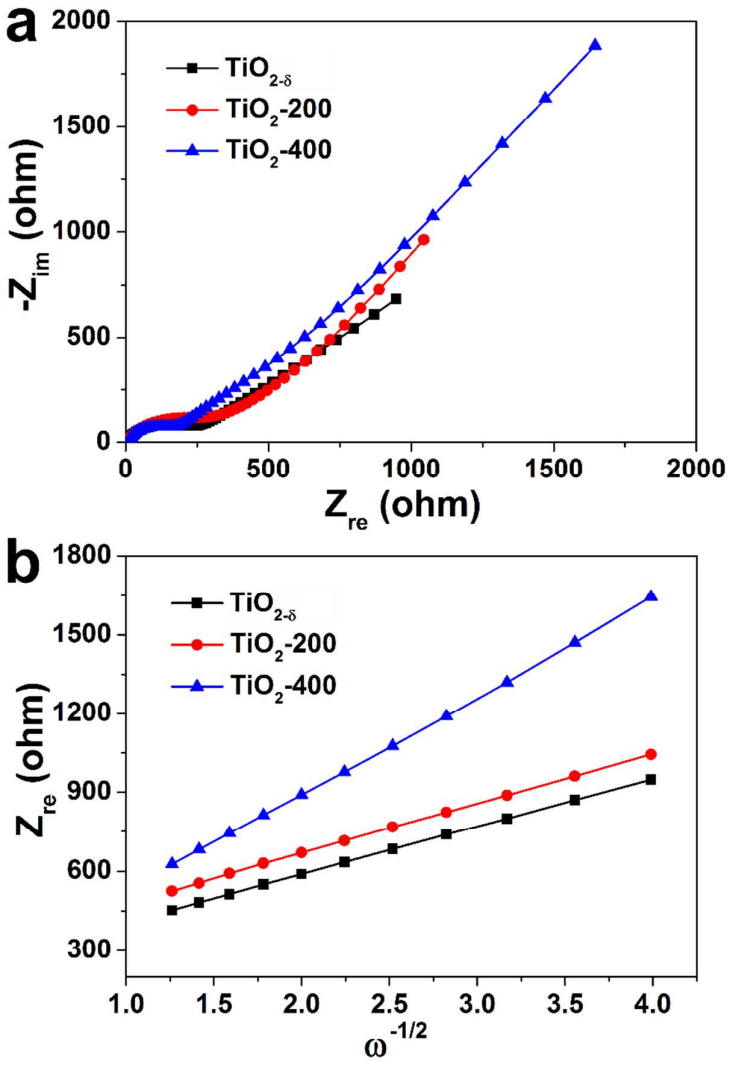

Figure S7. (a) Electrochemical impedance spectroscopy over the frequency range from 100 kHz to 10 mHz, (b) the relationship between Z_{re} and $\omega^{-1/2}$ within frequency of 0.1-0.01 Hz.

In the Nyquist plots, the inclined line in low frequency region represents the Warburg impedance associated with Li^+ diffusion in the solid phase. The Warburg coefficient σ, which is inversely proportional to $D^{1/2}$ ($D \propto 1/\sigma^2$), is defined as the slope of the fitting line of the relationship between Z_{re} and $\omega^{-1/2}$ ($Z_{re} \propto \sigma\omega^{-1/2}$) within 0.1~0.01 Hz.[2] We can observe that the slope of $TiO_{2-\delta}$ and TiO_2-200 is smaller than that of the TiO_2-400, indicating the amorphous TiO_2 is more favorable for Li diffusion in comparison with crystalline TiO_2.

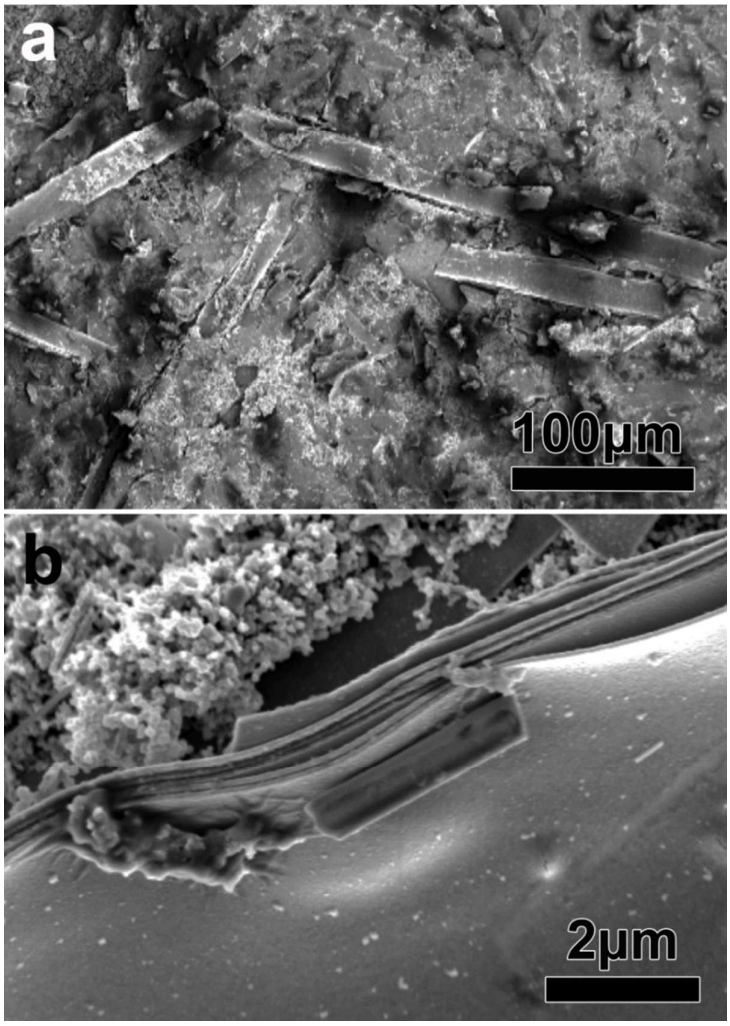

Figure S8. *Ex situ* SEM images of the $TiO_{2-\delta}$ nanomembranes after 100 cycles at 1C: (a) low magnification SEM image, (b) high magnification SEM image, exhibiting clear multi-windings with no appreciable structural damage.

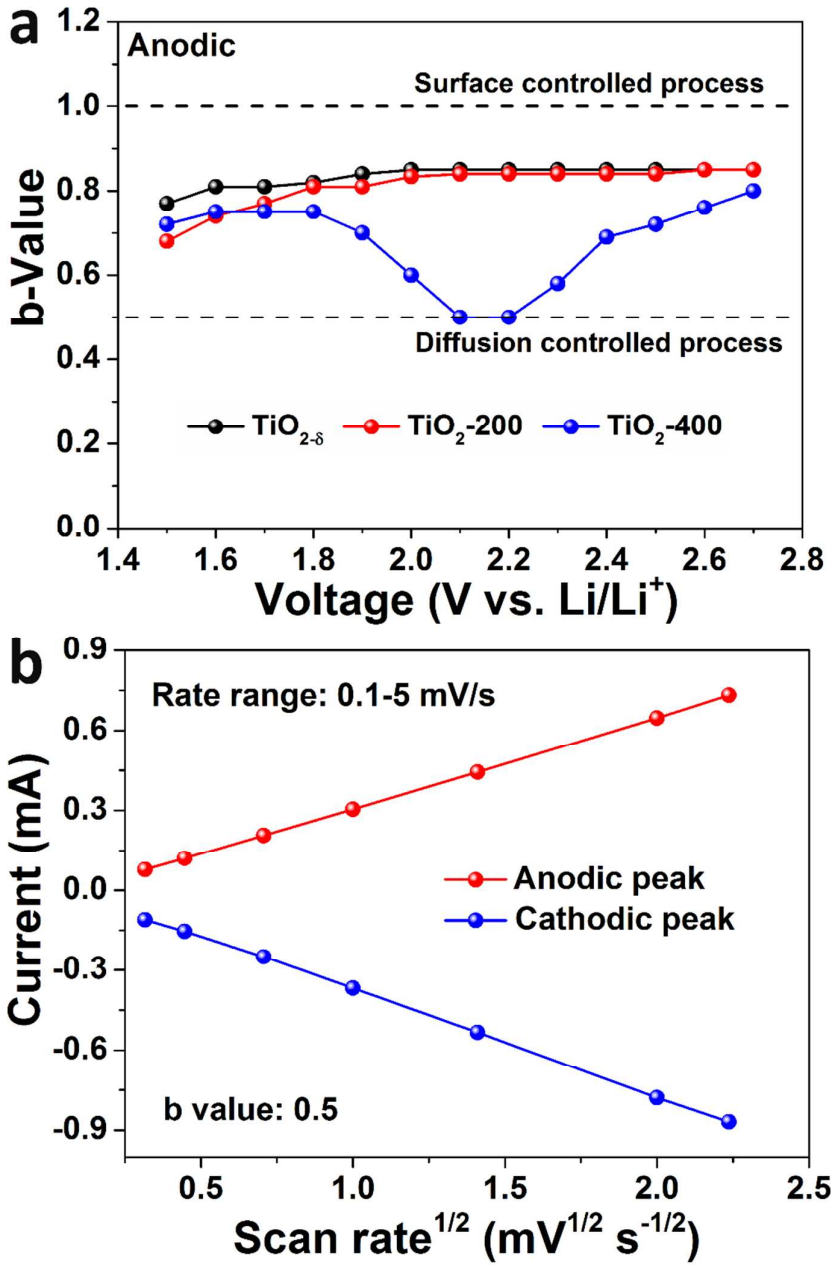

Figure S9 (a) The b-value determinations at different potentials for anodic sweep, (b) the peak current of TiO_2-400 *versus* square root of sweep rate (b=0.5).

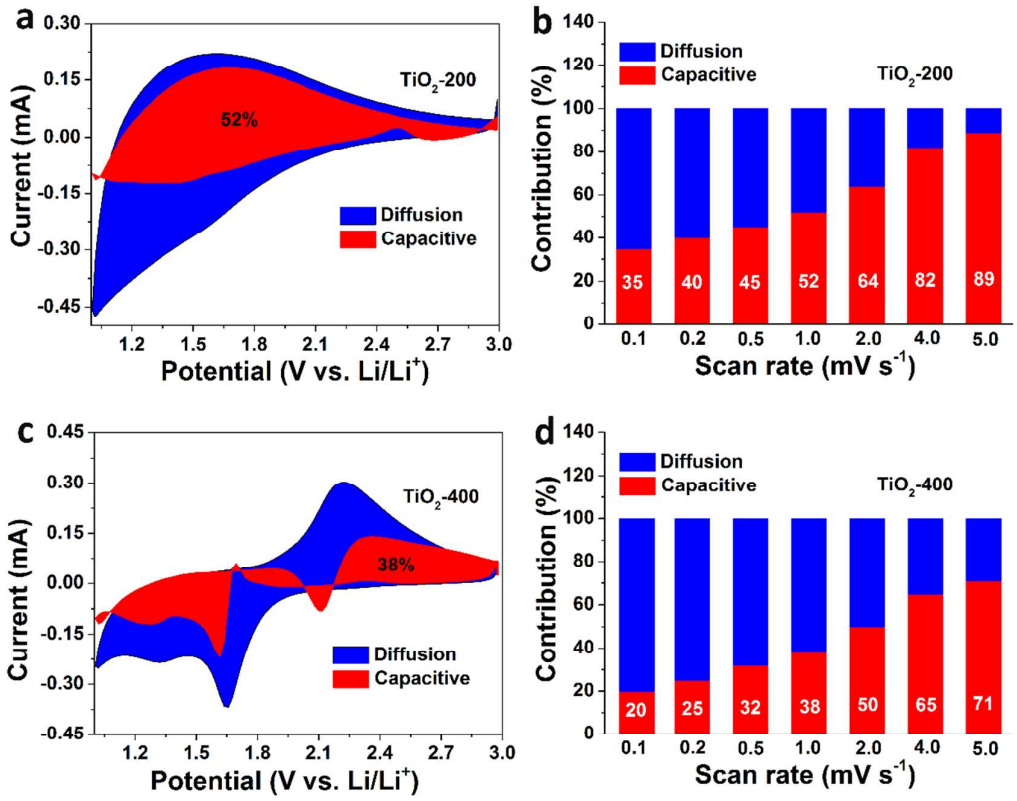

Figure S10. Capacitive (red) and diffusion-controlled (blue) contribution to the total charge storage at 1 mV s^{-1}: TiO_2-200 (a) and TiO_2-400 (c). Normalized contribution ratio of capacitive (red) and diffusion-controlled (blue) capacities at different rates: TiO_2-200 (b) and TiO_2-400 (d). The ratios of Li-ion capacitive contribution can be further quantitatively quantified by separating the current response i at a fixed potential V into capacitive effects (proportional to the scan rate ν) and diffusion-controlled reactions ($k_2\nu^{1/2}$), according to:[3, 4] $I(V) = k_1\nu + k_2\nu^{1/2}$, where ν is the sweep rate. By determining both k_1 and k_2 constants, we can distinguish the fraction of the current from surface capacitance and Li semi-infinite linear diffusion.

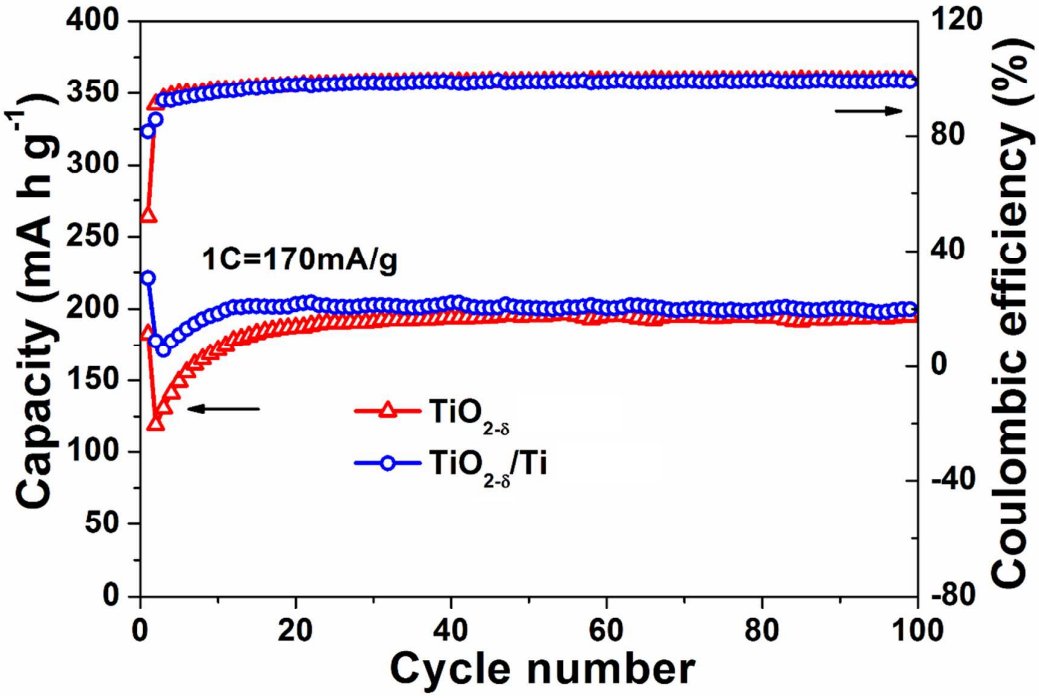

Figure S11. Cycling performances of $TiO_{2-\delta}$ and $TiO_{2-\delta}$/Ti nanomembranes at the rate of 1C.

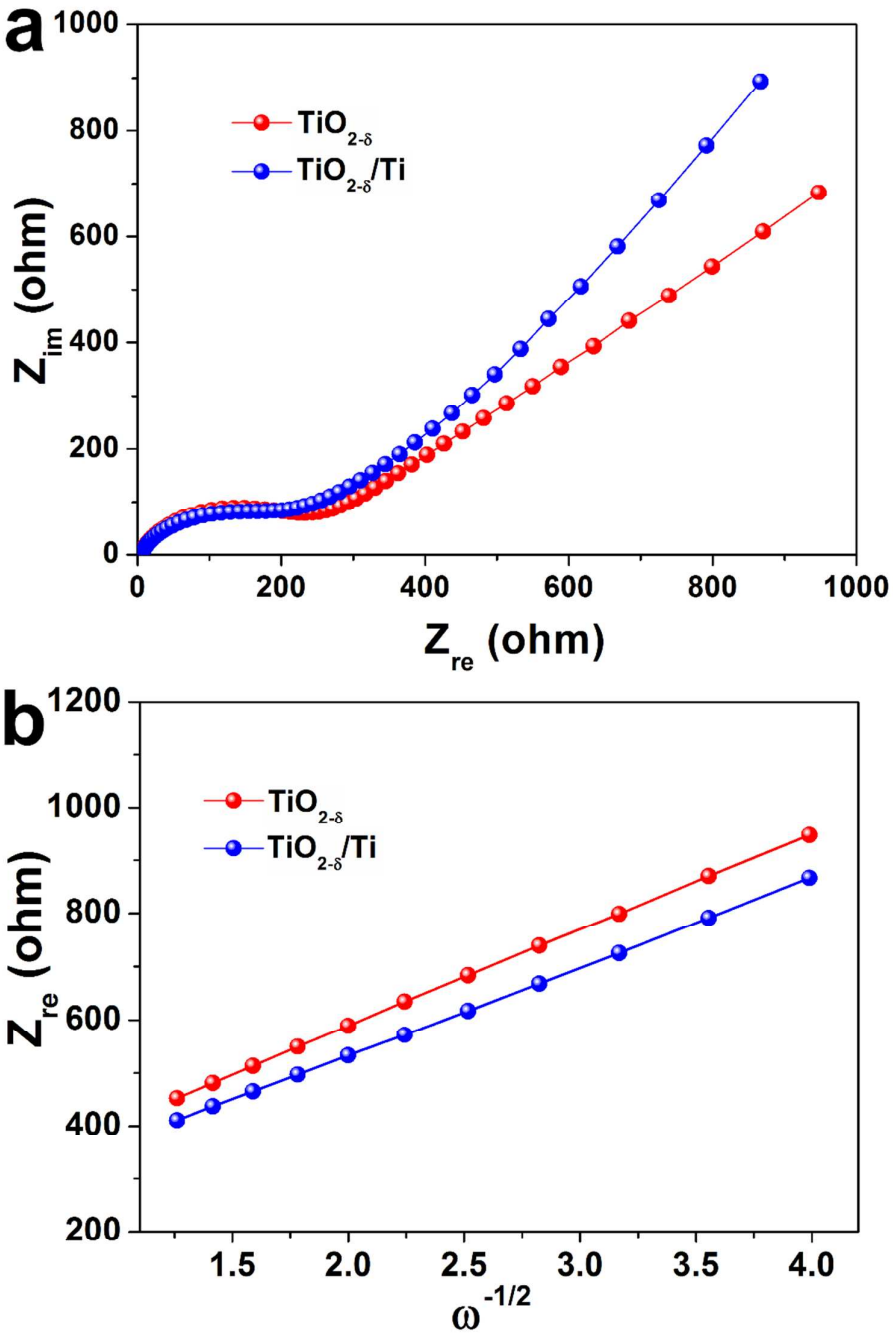

Figure S12. (a) Nyquist plots of $TiO_{2-\delta}$ and $TiO_{2-\delta}$/Ti over the frequency range from 100 kHz to 10 mHz, (b) the relationship between Z_{re} and $\omega^{-1/2}$ within frequency of 0.1-0.01 Hz.

Table S1. Comparison of lithium storage capacity of various TiO_2-based materials. Note that, to date, most of the successful TiO_2 nanostructures were chemically synthesized by hydro/solvothermal methods.

TiO_2 materials	**Electrochemical performance**	**Ref.**
Ti^{3+} Self-Doped TiO_2	**1 C: 200 mAh g^{-1}; 5000 cycles (10 C)**	**This work**
Anatase@Oxynitride/Titanium Nitride-GS	1 C: 166 mAh g^{-1}	5
Nanoporous Anatase TiO_2	1 C: 190 mAh g^{-1}	6
Anatase TiO_2 Hollow Spheres	1 C: 147.6 mAh g^{-1}	7
Anatase TiO_2 Quantum-Dot/Graphene-Nanosheet	1 C: 190 mAh g^{-1}	8
Rutile TiO_2 Submicroboxes	1 C: 188 mAh g^{-1}	9
Faceted TiO_2 Crystals	1 C: 141.2 mAh g^{-1}	10
Mesoporous TiO_2 hollow spheres	1 C: 175 mAh g^{-1}	11
Mesoporous TiO_2 Nanowire Bundles	1 C: 188 mAh g^{-1}	12
TiO_2 microboxes	1 C: 187 mAh g^{-1}	13

Reference:

(1) Villa, S.; Caratto, V.; Locardi, F.; Alberti, S.; Sturini, M.; Speltini, A.; Maraschi, F.; Canepa, F.; Ferretti, M. Enhancement of TiO_2 NPs Activity by Fe_3O_4 Nano-Seeds for Removal of Organic Pollutants in Water. *Mater.* **2016,** *9*, 771.

(2) Wu, X. L.; Guo, Y. G.; Su, J.; Xiong, J. W.; Zhang, Y. L.; Wan, L. J. Carbon-Nanotube-Decorated Nano-$LiFePO_4$@C Cathode Material with Superior High-Rate and Low-Temperature Performances for Lithium-Ion Batteries. *Adv. Energy Mater.* **2013,** *3*, 1155-1160.

(3) Brezesinski, T.; Wang, J.; Tolbert, S. H.; Dunn, B. Ordered Mesoporous [alpha]-MoO_3 with Iso-Oriented Nanocrystalline Walls for Thin-Film Pseudocapacitors. *Nat. Mater.* **2010,** *9*, 146-151.

(4) Chao, D.; Zhu, C.; Yang, P.; Xia, X.; Liu, J.; Wang, J.; Fan, X.; Savilov, S. V.; Lin, J.; Fan, H. J. Array of Nanosheets Render Ultrafast and High-Capacity Na-Ion Storage by Tunable Pseudocapacitance. *Nat. Commun.* **2016,** *7*, 12122.

(5) Qiu, Y.; Yan, K.; Yang, S.; Jin, L.; Deng, H.; Li, W. Synthesis of Size-Tunable Anatase TiO_2 Nanospindles and Their Assembly into Anatase@Titanium Oxynitride/Titanium Nitride-Graphene Nanocomposites for Rechargeable Lithium Ion Batteries with High Cycling Performance. *ACS Nano* **2010,** *4*, 6515-6526.

(6) Shin, J. Y.; Samuelis, D.; Maier, J. Sustained Lithium-Storage Performance of Hierarchical, Nanoporous Anatase TiO_2 at High Rates: Emphasis on Interfacial Storage Phenomena. *Adv. Funct. Mater.* **2011,** *21*, 3464-3472.

(7) Zhang, G.; Wu, H. B.; Song, T.; Paik, U.; Lou, X. W. D. TiO_2 Hollow Spheres Composed of Highly Crystalline Nanocrystals Exhibit Superior Lithium Storage Properties. *Angew. Chem. Int. Ed.* **2014,** *53*, 12590-12593.

(8) Mo, R.; Lei, Z.; Sun, K.; Rooney, D. Facile Synthesis of Anatase TiO_2 Quantum-Dot/Graphene-Nanosheet Composites with Enhanced Electrochemical Performance for Lithium-Ion Batteries. *Adv. Mater.* **2014,** *26*, 2084-2088.

(9) Yu, X. Y.; Wu, H. B.; Yu, L.; Ma, F. X.; Lou, X. W. D. Rutile TiO_2 Submicroboxes with Superior Lithium Storage Properties. *Angew. Chem. Int. Ed.* **2015,** *54*, 4001-4004.

(10) Liu, G.; Yin, L. C.; Pan, J.; Li, F.; Wen, L.; Zhen, C.; Cheng, H. M. Greatly Enhanced Electronic Conduction and Lithium Storage of Faceted TiO_2 Crystals Supported on Metallic Substrates by Tuning Crystallographic Orientation of TiO_2. *Adv. Mater.* **2015,** *27*, 3507-3512.

(11) Liu, H.; Li, W.; Shen, D.; Zhao, D.; Wang, G. Graphitic Carbon Conformal Coating of Mesoporous TiO_2 Hollow Spheres for High-Performance Lithium Ion Battery Anodes. *J. Am. Chem. Soc.* **2015,** *137*, 13161-13166.

(12) Jin, J.; Huang, S. Z.; Liu, J.; Li, Y.; Chen, L. H.; Yu, Y.; Wang, H. E.; Grey, C. P.; Su, B. L. Phases Hybriding and Hierarchical Structuring of Mesoporous TiO_2 Nanowire Bundles for High-Rate and High-Capacity Lithium Batteries. *Adv. Sci.* **2015,** *2,* 1500070

(13) Gao, X.; Li, G.; Xu, Y.; Hong, Z.; Liang, C.; Lin, Z. TiO_2 Microboxes with Controlled Internal Porosity for High-Performance Lithium Storage. *Angew. Chem. Int. Ed.* **2015,** *54*, 14331-14335.